Imaging Measurements and LES-CMC Modeling of a Partially-Premixed Turbulent Dimethyl Ether/Air Jet Flame

Bruno Coriton[1], M. Zendehdel[2], S. Ukai[2], A. Kronenburg[2], O. T. Stein[2], Seong-Kyun Im[3], Mirko Gamba[3,+], and Jonathan H. Frank[1,]*

[1]Combustion Research Facility, Sandia National Laboratories, Livermore, CA 94551, USA
[2] Institut für Technische Verbrennung, Universität Stuttgart, 70174 Stuttgart, Germany
[3]Dept. of Mechanical Engineering, Stanford University, Stanford, CA 94305 USA
[+](Current Address) Dept. of Aerospace Engineering, University of Michigan, Ann Arbor, MI 48109

Colloquium on Turbulent Flames
** Corresponding Author: Jonathan H. Frank*
P.O. Box 969, MS. 9053
Livermore, CA 94551, USA
Fax: (925) 294-2595
jhfrank@sandia.gov

Color reproduction charges will be paid for those figures that in the revision stage cannot be reproduced in black and white without loss of clarity.

main text					**4071**
references	**29**			equiv. words	**542**
	Figure			**Caption**	**Figure total**
	height [mm]	# columns	equiv. words		
Fig. 1	44	1	120	19	139
Fig. 2	100	1	242	30	272
Fig. 3	77	1	191	18	209
Fig. 4	76	1	190	13	203
Fig. 5	76	1	189	13	202
Fig. 6	55	1	143	15	158
All figures					**1183**
Total					**5796**

Imaging Measurements and LES-CMC Modeling of a Partially-Premixed Turbulent Dimethyl Ether/Air Jet Flame

Bruno Coriton[1], M. Zendehdel[2], S. Ukai[2], A. Kronenburg[2], O. T. Stein[2], Seong-Kyun Im[3], Mirko Gamba[3,+], and Jonathan H. Frank[1,]*

[1]Combustion Research Facility, Sandia National Laboratories, Livermore, CA 94551, USA

[2]Combustion Institut fuer Technische Verbrennung, Universitaet Stuttgart, 70174 Stuttgart, Germany

[3]Dept. of Mechanical Engineering, Stanford University, Stanford, CA 94305 USA

[+](Current Address) Dept. of Aerospace Engineering, University of Michigan, Ann Arbor, MI 48109

Turbulent dimethyl ether (DME) jet flames provide a canonical flame geometry for studying turbulence-flame interactions in oxygenated fuels and for developing predictive models of these interactions. The development of accurate models for DME/air flames would establish a foundation for studies of more complex oxygenated fuels. We present a joint experimental and computational investigation of the velocity field and OH and CH_2O distributions in a piloted, partially-premixed turbulent DME/air jet flame with a jet exit Reynolds number, Re_D, of 29,000. The turbulent DME/air flame is analogous to the well-studied, partially-premixed methane/air jet flame, *Sandia Flame D*, with identical stoichiometric mixture fraction, $\xi_{st} = 0.35$, and bulk jet exit velocity, $V_{bulk} = 45.9$ m/s. The results of the LES-CMC simulations performed on an intermediate size grid of

1.3 million cells are in good agreement with particle image velocimetry (PIV) and simultaneous CH_2O and OH laser-induced fluorescence (LIF) imaging measurements. LES-CMC simulations employing two different chemical reaction mechanisms (Kaiser *et al.*, 2000 and Zhao *et al.*, 2008) show approximately a factor of two difference in the peak CH_2O mole fractions, whereas OH mole fractions are in good agreement between the two mechanisms. The simultaneous OH-LIF and CH_2O-LIF measurements show a wide range of separation distances between the spatial distributions of these intermediate species, indicating that the consumption rates of formaldehyde by OH in a turbulent DME/air jet flame may be highly intermittent with significant departures from flamelet models.

Keywords: DME, Turbulent Jet Flames, PIV, LES-CMC, TNF workshop.

1. Introduction

Dimethyl ether (DME) is a promising clean fuel alternative for use in ground transportation compression ignition (CI) engines. DME's high cetane number and easy vaporization also make it a potential fuel candidate for homogeneous charge compression ignition (HCCI) engines [1]. DME-fueled engines have the potential of significantly reducing CO and soot emission levels because of the presence of oxygen in the DME molecule (CH_3–O–CH_3) and the absence of carbon-carbon bond [2, 3]. Despite the potential of DME as a clean fuel, appropriate combustion technologies must be developed and a fundamental understanding of the interplay between DME chemistry and turbulence is required.

Turbulent jet flames provide a canonical geometry in which to study turbulence-flame interactions and have been used in the development and testing of turbulent combustion models. Within the context of the International Workshop on Measurements and Computation of Turbulent Non-Premixed Flames

(TNF) [4], the piloted methane/air jet flames (Sandia flames C-to-F) spanning Reynolds number of approximately 13,000 to 43,000 have been used extensively for experimental studies (e.g. [5, 6]) and for model development (e.g. [7, 8]). DME flames represent a step forward in chemical complexity and a good starting point for systematic studies of turbulent flames with oxygenated fuels.

The present study is a joint experimental and computational investigation of the structure of a piloted, partially-premixed turbulent DME/air jet flame with respect to the OH and CH_2O fields. In DME combustion, the production of CH_2O is directly linked to the fuel consumption pathway, which results in significantly different distributions of CH_2O in DME jet flames than in methane jet flames [9]. We investigate the ability of an intermediate-resolution LES calculation to capture the distributions of CH_2O and OH, and we compare results of simulations using two different chemical mechanisms for DME combustion.

The partially-premixed DME/air turbulent jet flame with a jet exit Reynolds number of 29,000 is analogous to the well-studied *Sandia Flame D* [4, 5] with identical bulk jet exit velocity, V_{bulk}, of 45.9 m/s and stoichiometric mixture fraction, ξ_{st}, of 0.35. Recently, Fuest et al. [10] discussed the diagnostics challenges of Raman/Rayleigh scattering measurements in DME flames. In the present study, we use laser-induced fluorescence (LIF) imaging to measure the topology of the OH and CH_2O fields complemented by stereoscopic particle image velocimetry (SPIV) measurements of the velocity field.

The turbulent partially-premixed DME jet flame is simulated using a large eddy simulation combined with conditional moment closure, LES-CMC. LES resolves the largest turbulent structures and reverts to modeling for the small universal scales. The approach has been successfully used to model the related CH_4/air piloted jet flame series employing various different turbulent combustion models by, among others, Refs. [8, 11]. CMC is based on the notion that fluctuations of the reacting scalars are closely linked to the fluctuations of a small set of scalar reference variables [12], where for non-premixed flames usually the mixture fraction is employed. LES-CMC has been successfully used

to predict a number of target gas flames [13-15] and has recently been extended to multi-phase combustion [16, 17]. A previous application of LES-CMC to the piloted CH_4/air flame series has been reported by Navarro-Martinez et al. [18], where good agreement with the experimental data was found and closure models for the unclosed terms in the LES-CMC equations were proposed. In the present paper, the previously employed LES-CMC model is used without modification of any of the sub-models or model parameters, and applied to the piloted DME/air jet flame to test its predictive capability under modified combustion chemistry.

2. Experimental Methods

2.1. Piloted Jet Burner and Experimental Conditions

The partially-premixed DME/air flame was stabilized on a piloted jet burner with a central jet diameter of 7.45 mm (as opposed to 7.2 mm in previous Sandia CH_4/air Flame series), a pilot annulus of 18.2 mm and a coflow diameter of 254.0 mm. The annular pilot reactant mixture is composed of C_2H_2, H_2, CO_2, N_2 and air of equivalence ratio $\varphi_{pilot} = 0.6$. The pilot and mean jet flow rates are scaled proportionally such that the energy release of the pilot is approximately 2% of the main jet for each flame, as opposed to 6% in the Sandia CH_4/air flames. The burner is surrounded with an air coflow with an initial velocity of 0.9 m/s, monitored using a hot-film anemometer.

Mass flow controllers were used to regulate the gas supply to the jet and pilot and calibrated using piston-displacement calibration units (Sierra CalTrak) with accuracy of ±0.25% of the flow rate. DME was supplied in pressurized liquid tanks, preheated to 60C to ensure a steady supply of gas. At ambient temperature and atmospheric pressure, DME is stable in the gas phase. Preheating of the DME liquid tank did not affect the jet inlet temperature of 294K.

2.2. Stereo Particle Image Velocimetry (SPIV)

The SPIV system consisted of a dual-head Nd:YAG laser that provided a pair of laser pulses (λ=532 nm) separated by 4.0 μs at a repetition rate of 5 Hz. A combination of cylindrical lenses was used to expand and shape the laser beam into an approximately 1.0 mm thick laser sheet. Both jet and coflow were seeded with 0.3 μm aluminum oxide particles for the PIV measurements. Particle light scattering was imaged onto a pair of interline transfer CCD cameras mounted on the same side of the laser sheet at 23 degrees with respect to the normal of the imaging plane. The cameras were equipped with Nikon 105-mm f/2.8 macro lenses and Scheimpflug mounts to compensate for the displacement of the imaging plane. A narrow-bandwidth interference filter centered at 532 nm was also placed in front of the lens to reduce interference from flame luminosity.

Velocity vectors were calculated using an iterative cross-correlation processing algorithm with final interrogation window size of 32x32 px^2 and 50% overlapping, resulting in a vector spacing of 237 μm. A universal outlier detection algorithm was used to eliminate spurious vectors that were discarded in the computation of the velocity statistics. No smoothing was applied to the velocity vector fields.

2.3. Simultaneous OH-LIF and CH_2O-LIF Imaging

Laser-induced fluorescence of OH was excited by the frequency doubled output of a Nd:YAG-pumped dye laser tuned to the $Q_1(6)$ line (λ=283.01 nm, ~1.2mJ/pulse) of the $A^2\Sigma^+ \leftarrow X^2\Pi^+(v'=1,v''=0)$ band of OH. The OH fluorescence emission from the A-X(0,0) and (1,1) bands was imaged onto an intensified CCD camera using a UV-camera lens (f.l.=45 mm, f/1.8) with color glass filters (UG11 and WG305) to block interferences. The OH-LIF measurements were corrected for spatial variations in the average dye-laser beam profile and the throughput of the imaging system. Shot-to-shot fluctuations were negligible for the subsection of the dye-laser beam that was used for LIF imaging. The OH-LIF signals were not corrected for local variations in quenching rates and the OH ground-state Boltzmann fraction population.

Laser-induced fluorescence of formaldehyde was excited by the third harmonic of an injection seeded Nd:YAG laser (~42 mJ/pulse). The diode seed laser was temperature tuned to λ=354.83 nm to excite overlapping transitions in the 4_0^1 band of the $\tilde{A}^1A_2 \leftarrow \tilde{X}^1A_1$ system. The CH_2O fluorescence emission was imaged onto an intensified CCD camera using a medium-format camera lens, an AR-coated singlet (f.l.=-400 mm), and a 35-mm format lens. A color glass filter (GG375) in the imaging system blocked elastic scattering from the laser and transmitted the CH_2O-LIF signal. The laser beam was horizontally polarized to eliminate interferences from Rayleigh or Raman scattering.

3. Numerical Methods

3.1. LES-CMC Modeling

Combustion was modeled by coupling the CMC method with LES, as described in Ref. [18], with the CMC grid coarser than the LES mesh. The conditional moments of the reacting species mass fractions and enthalpy were solved conditional on mixture fraction. LES-CMC requires a number of closure assumptions. Following Ref. [18], the shape of the filtered-density function (FDF) was presumed as a β-function and the conditional fluctuations were assumed negligible in the modeling of the conditional reaction source terms (first-order CMC). The conditionally-filtered scalar dissipation, velocity and diffusivity required in the CMC equations were modeled as simple ensemble averages of the filtered dissipation, velocity and turbulent diffusivity, conditioned on filtered mixture fraction within a CMC cell. DME/air combustion chemistry was represented by two different reaction mechanisms, namely Fischer/Kaiser *et al.* [19, 20] consisting of 78 species and 351 reactions and Zhao *et al.* [21] employing 55 species and 290 reactions. These two mechanisms are referred to as *Kaiser* and *Zhao* mechanisms, respectively.

A density-weighted Favre-filter was used to derive the filtered Navier-Stokes equations. The subgrid stresses were modeled based on the eddy viscosity approach and the turbulent viscosity was

modeled using Smagorinsky's model [22] with the model constant adjusted dynamically [23]. To account for turbulent mixing between fuel and oxidizer, an additional mixture fraction transport equation was solved, with the subgrid scalar flux modelled by assuming gradient diffusion and a turbulent Schmidt number of 0.4. The LES equations were solved using a SIMPLE-type predictor-corrector method with pressure smoothing as described in Ref. [24].

The in-house LES-CMC code BOFFIN was used for the simulations. A stretched Cartesian mesh was employed, where the computational domain of 10Dx10D at the inlet plane was expanded towards the domain outlet to account for the radial jet spreading. The domain extended over 60D in the downstream direction. A constant LES grid resolution of 72x72x240 cells was used, according to previous grid independence studies in the CH_4/air flame series. A CMC grid resolution of 2x2x60 cells was employed, where again prior experience from the CH_4/air flame shows that this shear layer dominated flame can be captured with a relatively coarse CMC resolution in the cross-stream direction. At the inlet plane, artificially generated turbulence was superimposed to the mean velocity profile following Klein *et al.* [25], which requires a nominal integral length scale and Reynolds-stress tensor as inputs. The integral scale was assumed to be 0.25D and the Reynolds-stress tensor was set to match the mean and RMS axial velocity profiles measured 1 mm above the nozzle exit. Coflow inflow conditions were matched to the experiments and a zero-gradient boundary condition was set at the exit plane. To achieve statistical convergence, the simulations were run in parallel using MPI for approximately 4 weeks on 48 AMD-Opteron cores.

3.2. Simulation of LIF Signals

A comparison of the calculated and measured distributions of CH_2O and OH was performed by using instantaneous realizations of the temperature and species mole fractions from the LES calculation to simulate the LIF signals. Simulation of the LIF signals requires knowledge of the temperature dependence of the Boltzmann fraction population of the ground state and the collisional quenching rates

of the excited state. For simulating OH-LIF signals, we calculated the Boltzmann fraction population of the $Q_1(6)$ transition of the $A^2\Sigma^+ \leftarrow X^2\Pi^+$ (v'=1,v"=0) band and the quenching rates using the quenching cross sections from Tamura et al.[26].

The simulation of formaldehyde LIF signals is more complex than OH because of the high spectral density of transitions and the lack of available quenching cross sections at flame temperatures. The density of active transitions increases at elevated temperatures. The temperature dependent populations of the lower states of the relevant overlapping transitions in the 4_0^1 band of the $\tilde{A}^1A_2 \leftarrow \tilde{X}^1A_1$ system were calculated using Asyrot spectral simulation software [27]. For the quenching rate calculations, we compared two different models for the temperature dependence of quenching cross-sections. In one model, the quenching cross-sections of all species were considered to be independent of temperature, and in the second model a power law of $T^{-0.5}$ was used [28]. An example of the predicted LIF signals using $T^{-0.5}$ dependence is shown in Fig. 1 for a laminar counterflow flame calculation with the same fuel stream composition as the turbulent jet flame. The laminar flame calculation was performed using Chemkin Oppdiff [29] and the Zhao and Kaiser DME mechanisms for a strain rate of a=200 s^{-1}. The CH_2O LIF profiles are biased towards lower temperatures and their peaks are shifted by approximately 0.25 mm with respect to the CH_2O mole fraction peaks. The peak LIF signal for the Zhao mechanism is approximately 34% larger than that of the Kaiser mechanism, and the peak mole fractions differ by 29%. The peak CH_2O LIF signal using temperature-independent quenching cross sections (not shown) was slightly shifted 0.04 mm towards lower temperatures. For comparisons of the LES with measurements in the turbulent flame, we used the $T^{-0.5}$ dependence. An example of instantaneous measured and computed LIF signals in the turbulent jet flame is shown in Fig. 2.

4. Results and Discussion

4.1. Velocity Statistics

Figure 3 shows radial profiles of the measured and computed mean and root-mean-squared (RMS) velocity from x/D=5 to 25. Note that in addition to temporal averaging over a large number of steady-state realizations, the statistical convergence of the 3D-LES velocity data was improved by averaging along the circumference of the axisymmetric configuration. The velocity profiles for the simulations using different mechanisms are virtually identical. The mean measured and computed velocity profiles match very well at most downstream positions, despite some minor off-axis discrepancies. The measured and computed RMS velocities are in good agreement. The centerline RMS velocities match at x/D=5, apart from a slight inward shift of the LES data, which may stem from difficulties in resolving the steep upstream shear layer. The measurements show a slower increase in the centerline RMS velocity as a function of downstream position. The measured and computed locations of the peak RMS velocity are also slightly different near the nozzle but shows closer agreement with increasing downstream position. Measurements of the radial and azimuthal, mean and RMS velocity components (not shown) agreed well with the LES-CMC simulations.

4.2. OH and CH_2O Field Statistics

For the turbulent jet flame, we compare the measured and computed radial profiles of OH and CH_2O LIF signals. The computed LIF signals from the LES-CMC results from the Zhao and Kaiser mechanisms were calculated using 656 and 555 instantaneous realizations, respectively. For each realization, the LIF signals were computed from the mole fractions of OH, CH_2O, major species and the temperature using the approach described in Section 3.2. The comparison is initiated by normalizing the peak values of the measured and computed LIF signals at the position nearest to the nozzle exit, x/D=5. The mean OH-LIF profiles in Fig. 4 show the progression of the radial distribution of OH from x/D=5 to 25, with negligible differences between the two mechanisms. At the farthest downstream positions, the

experimental data are truncated at the largest radial positions due to the limited extent of the measurement. Overall, the agreement between the experiment and simulation is quite good. At x/D=5, the peak location of experiment and computation are near r/D=1. The experiment and simulation show a similar progression of increasing width and radial location of the peaks with downstream position. The computed OH-LIF profiles are consistently more skewed towards larger radial positions. The peak location in the measurement is slightly closer to the jet axis for x/D=5-15. The profiles of RMS OH-LIF signals in Fig. 4 use the normalization factor from the mean OH-LIF profile at x/D=5. The measured and computed RMS profiles exhibit similar bimodal structure at x/D=5-15 with the measured values somewhat larger than the computed profiles. Overall, the agreement in the radial position and shape of the RMS OH-LIF profiles is quite good.

The measured and computed CH_2O-LIF profiles are shown in Fig. 5. The measured profiles are plotted twice in Fig.5 with separate normalization to the computed profiles for each reaction mechanism at x/D=5. Overall, the computed CH_2O-LIF signals for both reaction mechanisms are in good agreement with the normalized experimental data, with no significant improvement of using one reaction mechanism over the other. The mean CH_2O-LIF radial profiles have a peak off the jet centerline for axial locations x/D=5-15 and transition to having a peak on the jet axis at x/D=20 and 25. As the axial location increases, the measured CH_2O-LIF profiles spread faster and extend to increasingly larger radial positions than the computed CH_2O-LIF profiles. The measured and computed radial profiles of RMS CH_2O-LIF signals evolve quite similarly with bimodal distributions at x/D=5 and 10 and single off-axis peaks at x/D=15-25. Similar to the mean profiles, the measured RMS profiles expand in the radial direction more than the computed profiles as the downstream position increases. Similar trends were observed when simulating CH_2O-LIF signals with temperature independent quenching cross sections.

The most noticeable difference between the CH_2O-LIF profiles using the different mechanisms is that the Zhao mechanism predicts a factor of approximately two higher peak CH_2O-LIF signals at all

axial locations. This difference is not an artifact of comparing LIF signals but is also observed in the LES predictions of mole fractions (not shown). The laminar flame calculations in Fig. 1 also showed a discrepancy between the mechanisms. This discrepancy may stem from a difference between the relative contributions of unimolecular decomposition and the abstraction of a hydrogen atom from DME in the fuel consumption pathway of each mechanism. A reaction pathway analysis from the laminar flame calculations shows that the dominant production reaction for formaldehyde in both mechanisms is the decomposition of the methoxy-methyl radical via the reaction $CH_3OCH_2 = CH_2O + CH_3$. The production of the methoxy-methyl radical from DME proceeds via abstraction of a hydrogen atom by reactions of DME with radicals, such as H, OH, O, CH_3. For both mechanisms, the dominant hydrogen atom abstraction reaction is $DME + H = CH_3OCH_2 + H_2$. However, the second most important DME consumption reaction differs for each mechanism. For the Kaiser mechanism, the second most important reaction is the unimolecular decomposition of DME via the reaction $DME = CH_3 + CH_3O$. In contrast, the second most important reaction for the Zhao mechanism is hydrogen abstraction via $DME + CH_3 = CH_3OCH_2 + CH_4$. As a result, the production of the methoxy-methyl radical and subsequently formaldehyde may be enhanced in the Zhao mechanism.

4.3. Structural Analysis of OH and CH_2O Distributions

A reaction rate analysis of formaldehyde consumption shows that the second most significant consumption reaction is $CH_2O + OH = HCO + H_2O$, with the first and third most significant being reactions of formaldehyde with atomic hydrogen and methyl radicals, respectively. The laminar flame calculations in Fig. 1 show that the tails of the formaldehyde and OH distributions overlap in the region where formaldehyde is consumed. In contrast, the single-shot measurements and the LES realization in Fig. 2 show that there can be wide separations between the OH layer and the outer boundary of the formaldehyde distribution in many regions of the turbulent jet flame. The single-shot measurement at x/D=5 (bottom right image) shows that a significant portion of the formaldehyde layer is in close

proximity to the OH layer on the right-hand side, although a pocket with a larger gap appears in the upper region of the image. The relative distributions evolve with downstream position. The formaldehyde distribution fills in along the centerline and broadens to increasing radial positions, and the OH layer broadens and becomes increasingly convoluted. At the farthest downstream positions, there is often a significant gap between the outer boundary of the formaldehyde distribution and the inner boundary of the OH layer. All of the single-shot measurements at x/D=5-25 show thin, horizontally-stretched layers of formaldehyde extending away from the jet centerline such that they are in close proximity to the OH layer.

To quantify the sizes of this gap on a statistical basis, we analyzed 700 simultaneous OH and CH_2O LIF images at each downstream location and measured the radial separation distance between the outer boundary of the formaldehyde distribution and the inner boundary of the OH layer. The measurement was performed in each image along every eighth row of pixels, which corresponded to a vertical sampling of approximately 150 μm. Figure 6 shows the probability density function (PDF) of the OH-CH_2O separation distance as a function of axial location. The PDFs, which have a bin size of 0.25 mm, show that the most probable separation distance is less than 0.50 mm at all axial locations. Note that the small probability of negative separation distances corresponds to locations where there is a slight overlap between the OH and CH_2O fields. The PDFs are asymmetric with tails that extend towards larger separation distances. There is a consistent progression of monotonically increasing probability of large gaps as a function of downstream location. At x/D=5, the tail of the PDF extends to a maximum gap of approximately 3.0 mm, whereas at x/D=25 the gap sizes are as large as 10 mm, which is approximately 1.3 nozzle diameters. The PDFs at x/D=20 and 25 diameters are very similar, suggesting that the distribution asymptotes near this location. The frequent lack of overlap in the instantaneous OH and CH_2O distributions may produce significant intermittency in the consumption rate of CH_2O by OH and may reduce the overall role of this reaction in the consumption of formaldehyde relative to that predicted by laminar flamelet models.

5. Conclusions

A joint experimental and computational study of a piloted, turbulent partially-premixed DME/air jet flame at a jet exit Reynolds number of 29,000 and a stoichiometric mixture fraction of 0.35 was performed with a focus on comparing the velocity, CH_2O, and OH fields. Velocity measurements were performed using stereo particle image velocimetry, and CH_2O and OH were imaged using laser-induced fluorescence at downstream locations of x/D=5-to-25. LES-CMC calculations on a domain extending up to x/D=60 were performed using approximately 1.3 million cells. The results show that this moderate resolution simulation agrees well with the measurements and captures much of the evolution of the mean and RMS velocity field, as well as the OH and CH_2O fields. To adequately compare the CH_2O and OH fields obtained from the LES-CMC simulations to the LIF measurements of CH_2O and OH, the CH_2O and OH LIF signals were calculated from the LES-CMC results and then compared directly to the measurements. Because of the lack of available CH_2O LIF quenching cross sections at flame temperatures, the cross sections were modeled as both temperature independent and with a $T^{-1/2}$ power law dependence. Simulations using the Zhao and Kaiser DME mechanisms showed little difference in the mean and RMS profiles of temperature, velocity, and OH. However, the Zhao mechanism predicted approximately a factor of two greater peak formaldehyde levels than the Kaiser mechanism. The LIF imaging measurements revealed that at many downstream locations, the instantaneous spatial distributions of these radicals can be separated by significant distances. The LES results also showed gaps between the OH and CH_2O distributions. These gaps may produce highly intermittent consumption rates of formaldehyde by OH and produce significant departures from flamelet models in turbulent jet flames.

Acknowledgments

The authors thank M.G. Mungal for contributions to the experiments, W.P. Jones for providing the original CFD routines, and E. Huang for technical assistance in the laboratory. The experimental

research was supported by the U.S. Department of Energy, Office of Basic Energy Sciences, Division of Chemical Sciences, Geosciences, and Biosciences. Sandia National Laboratories is a multiprogram laboratory operated by Sandia Corporation, a Lockheed Martin Company, for the U.S. Department of Energy under contract DE-AC04-94-AL85000. The Stuttgart group acknowledges the financial support of DFG (grant no. KR3648/1-2), high-performance computing access to HLRS. S.K. Im and M. Gamba were supported by the Department of Energy under Award Number DE-FC52-08NA28614.

References

[1] C. Arcoumanis, C. Bae, R. Crookes, E. Kinoshita, Fuel, 87 (2008) 1014-1030.
[2] X. Lu, D. Han, Z. Huang, Prog. Energy Combust. Sci., 37 (2011) 741-783.
[3] S.H. Park, C.S. Lee, Prog. Energy Combust. Sci., 39 (2013) 147-168.
[4] International Workshop on Measurement and Computation of Turbulent Nonpremixed Flames (TNF), http://www.sandia.gov/TNF
[5] R.S. Barlow, J.H. Frank, Proc. Combust. Inst., 27 (1998) 1087-1095.
[6] C. Schneider, A. Dreizler, J. Janicka, E.P. Hassel, Combust. Flame, 135 (2003) 185-190.
[7] J. Xu, S.B. Pope, Combust. Flame, 123 (2000) 281-307.
[8] A. Kempf, F. Flemming, J. Janicka, Proc. Combust. Inst., 30 (2005) 557-565.
[9] K.N. Gabet, H. Shen, R.A. Patton, F. Fuest, J.A. Sutton, Proc. Combust. Inst., 34 (2013) 1447-1454.
[10] F. Fuest, R.S. Barlow, J.-Y. Chen, A. Dreizler, Combust. Flame, 159 (2012) 2533-2562.
[11] H. Pitsch, H. Steiner, Phys. Fluids, 12 (2000) 2541-2554.
[12] A.Y. Klimenko, R.W. Bilger, Prog. Energy Combust. Sci., 25 (1999) 595-687.
[13] A. Garmory, E. Mastorakos, Proc. Combust. Inst., 33 (2011) 1673-1680.
[14] A. Triantafyllidis, E. Mastorakos, R.L.G.M. Eggels, Combust. Flame, 156 (2009) 2328-2345.
[15] S. Navarro-Martinez, A. Kronenburg, Flow Turbulence Combust, 87 (2011) 377-406.
[16] M. Mortensen, R.W. Bilger, Combust. Flame, 156 (2009) 62-72.
[17] S. Ukai, A. Kronenburg, O.T. Stein, Proc. Combust. Inst., 34 (2013) 1643-1650.
[18] S. Navarro-Martinez, A. Kronenburg, F. DiMare, Flow Turbulence Combust, 75 (2005) 245-274.
[19] S.L. Fischer, F.L. Dryer, H.J. Curran, Int. J. Chem. Kin., 32 (2000) 713-740.
[20] E.W. Kaiser, T.J. Wallington, M.D. Hurley, J. Platz, H.J. Curran, W.J. Pitz, C.K. Westbrook, J. Phys. Chem. A, 104 (2000) 8194-8206.
[21] Z. Zhao, M. Chaos, A. Kazakov, F.L. Dryer, Int. J. Chem. Kin., 40 (2008) 1-18.
[22] R. Sivaramakrishnan, J.V. Michael, A.F. Wagner, R. Dawes, A.W. Jasper, L.B. Harding, Y. Georgievskii, S.J. Klippenstein, Combust. Flame, 158 (2011) 618-632.
[23] U. Piomelli, J. Liu, Phys. Fluids, 7 (1995) 839-848.
[24] N. Branley, W.P. Jones, Combust. Flame, 127 (2001) 1914-1934.
[25] M. Klein, A. Sadiki, J. Janicka, J. Comput. Phys., 186 (2003) 652-665.
[26] M. Tamura, P.A. Berg, J.E. Harrington, J. Luque, J.B. Jeffries, G.P. Smith, D.R. Crosley, Combust. Flame, 114 (1998) 502-514.
[27] R.H. Judge, D.J. Clouthier, Comp. Phys. Comm., 135 (2001) 293-311.
[28] P.H. Paul, H.N. Najm, Proc. Combust. Inst., 27 (1998) 43-50.
[29] R.J. Kee, *et al.*, in, Reaction Design, Inc., San Diego, CA, 2007.

Figures

Figure 1. Laminar flame calculations of partially premixed DME/air flame using Zhao and Kaiser DME mechanisms and simulated CH_2O LIF signal.

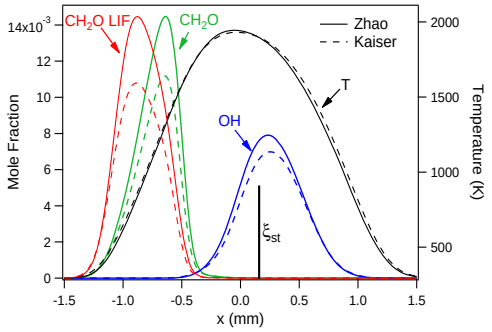

Figure 2. Composite image of computed OH-LIF and CH_2O-LIF signals from an instantaneous realization of the LES calculations (left). Composite images of single-shot OH-LIF and CH_2O-LIF measurements at different downstream positions (right).

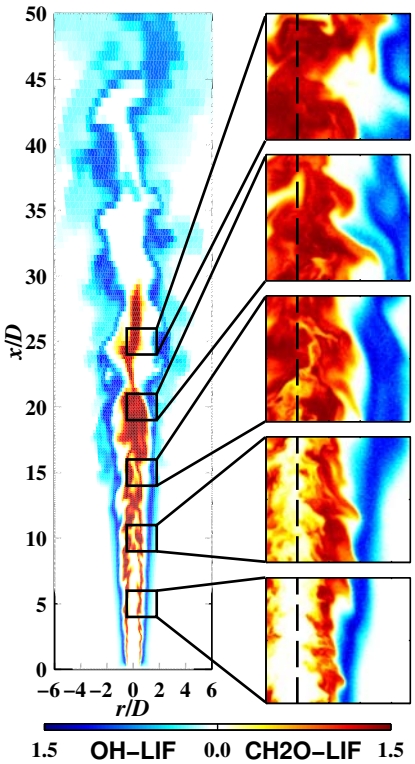

Figure 3. Measured (Exp.) and computed (LES) radial profiles of mean and RMS of axial velocity in DME jet flame.

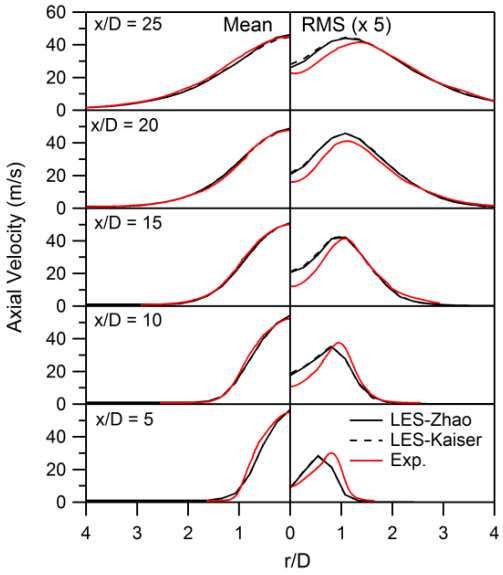

Figure 4. Measured (Exp.) and computed (LES) radial profiles of mean and RMS OH-LIF signals.

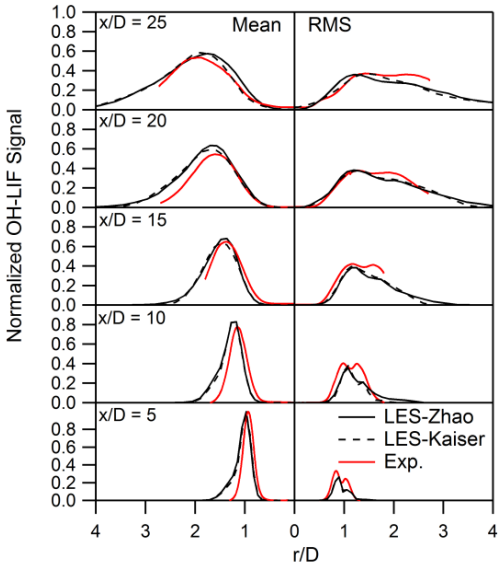

Figure 5. Measured (Exp.) and computed (LES) radial profiles of mean and RMS CH_2O-LIF signals.

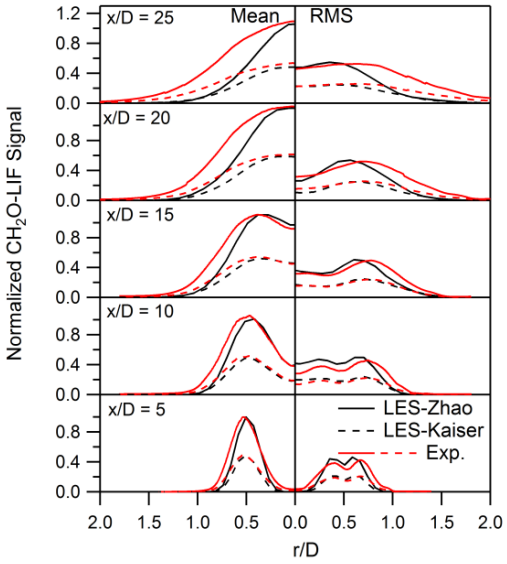

Figure 6. Probability density function of separation distance between the boundaries of the CH_2O and OH fields.

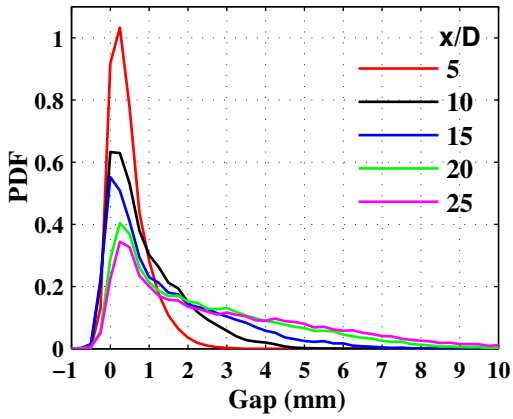

List of Figure Captions

Figure 1. Laminar flame calculations of partially premixed DME/air flame using Zhao and Kaiser DME mechanisms and simulated CH_2O LIF signal.

Figure 2. Composite image of computed OH-LIF and CH_2O-LIF signals from an instantaneous realization of the LES calculations (left). Composite images of single-shot OH-LIF and CH_2O-LIF measurements at different downstream positions (right).

Figure 3. Measured (Exp.) and computed (LES) radial profiles of mean and RMS of axial velocity in DME jet flame.

Figure 4. Measured (Exp.) and computed (LES) radial profiles of mean and RMS OH-LIF signals.

Figure 5. Measured (Exp.) and computed (LES) radial profiles of mean and RMS CH_2O-LIF signals.

Figure 6. Probability density function of separation distance between the boundaries of the CH_2O and OH fields.